Biophysical Journal Volume 105 October 2013 1805–1811

Mechanical Cues in the Early Embryogenesis of *Caenorhabditis elegans*

Rolf Fickentscher, Philipp Struntz, and Matthias Weiss*

Experimental Physics I, University of Bayreuth, Bayreuth, Germany

ABSTRACT Biochemical signaling pathways in developmental processes have been extensively studied, yet the role of mechanical cues during embryogenesis is much less explored. Here we have used selective plane illumination microscopy in combination with a simple mechanical model to quantify and rationalize cell motion during early embryogenesis of the small nematode *Caenorhabditis elegans*. As a result, we find that cell organization in the embryo until gastrulation is well described by a purely mechanical model that predicts cells to assume positions in which they face the least repulsive interactions from other cells and the embryo's egg shell. Our findings therefore suggest that mechanical interactions are key for a rapid and robust cellular arrangement during early embryogenesis of *C. elegans*.

INTRODUCTION

The development of body axes, polarized tissues, and organ precursors are central phenomena during embryogenesis. To explain these events, frequently a morphogen-driven patterning of organisms is considered: Morphogens may support the formation of Turing patterns (1), e.g., during skin patterning of zebrafish (2), whereas other scenarios like wing development in fruit flies do not seem to rely on Turing-like mechanisms but instead exploit a uniform morphogen expression (3). Although genetic screens and elaborate biochemical techniques have boosted our understanding of morphogen-triggered pathways during the development of tissues and organisms, the role of mechanical interactions between cells has been widely neglected for a long time. Indeed, examples of an active role of mechanical cues during developmental processes have been established only very recently (4–8). As of yet, however, our knowledge on how much of the developmental processes would be governed by mechanical rather than biochemical cues is still fragmentary. Such insights may also be crucial to integrate the different timescales observed in developmental systems: Whereas cell division and migration happen in a temporal range of many minutes up to hours (*Caenorhabditis elegans*, for example, progresses within ~1 h from the zygote to a state with ~20 cells), cellular signaling cascades are typically much faster, namely in the range of seconds to a few minutes (9).

For a long time a quantitative monitoring of developmental processes in real time has been hampered by the lack of gentle yet fast, three-dimensional fluorescence microscopy methods with a low phototoxicity, as would be required to not alter the development of embryos during extended observation periods. In the last decade, new imaging techniques have emerged that overcome this barrier. Presumably the most prominent technique in this context is light-sheet microscopy, often abbreviated as selective plane illumination microscopy (SPIM) (10–13). In SPIM approaches, a thin light sheet is formed by a cylindrical lens or by scanning a line with a focused laser beam to illuminate only a slice of a few micrometers thickness in the sample. Fluorescence from this illuminated slice is detected by a camera that is oriented perpendicular to the light sheet, i.e., all voxels in the illuminated sheet are imaged in parallel. Three-dimensional representations of the probe are achieved by moving sample and light sheet relative to each other. Several implementations of SPIM have been reported in recent years (see, e.g., Huisken and Stainier (14) for review). Common to all is a layer-wise, gentle illumination and a fast recording, i.e., phototoxicity is strongly reduced so that an unperturbed development of a living specimen can be monitored in three dimensions over extended timescales.

Here, we have used SPIM and a simple mechanical model to elucidate the influence of mechanical interactions between cells during early embryogenesis of the small, transparent nematode *Caenorhabditis elegans*. In particular, we imaged *C. elegans* embryos with a high spatial and temporal resolution to obtain tracks of individual cells during early embryogenesis. As a result, we found that these trajectories are remarkably conserved from embryo to embryo, hence suggesting a conserved and robust driving force of cell migration. Using a simple model that only includes mechanical/sterical interactions between cells, we were able to reliably predict the arrangement of cells up to the 12-cell stage, i.e., in stages before gastrulation. Notably, the model predicts the experimentally observed planar cell arrangement in the four-cell stage as well as the spontaneous formation of the dorsal-ventral body axis. Neglecting the cells' interaction with the egg shell of the embryo resulted in a T-like arrangement of cells that also has been observed experimentally (15). Thus, early *C. elegans* embryogenesis seems to rely on robust mechanical cues to arrange cells,

Submitted July 24, 2013, and accepted for publication September 11, 2013.

*Correspondence: matthias.weiss@uni-bayreuth.de

Rolf Fickentscher and Philipp Struntz have contributed equally to this work.

Editor: Jeffrey Fredberg.

0006-3495/13/10/1805/7 $2.00

http://dx.doi.org/10.1016/j.bpj.2013.09.005

whereas biochemical signaling events becomes increasingly important at and beyond the time point of gastrulation (16).

MATERIALS AND METHODS

Worm culture and sample preparation

Transgenic worm lines expressing GFP-tagged histones and β-tubulin (strain XA3501) were a kind gift of I. Mattaj (European Molecular Biology Laboratory, Heidelberg, Germany). Worms were cultured and dissected to extract early zygotes as described in Askjaer et al. (17) and Bao and Murray (18). After extraction, eggs were mounted rapidly in a 10–20 μL drop of M9 buffer with 0.5% low-melting agarose (Agarose Low Melt; Carl Roth, Karlsruhe, Germany). This sample was placed on top of a 2% low-melting agarose cushion (~30 μL) previously mounted on a coverslip. As a result, reflections from the coverslip were greatly reduced. Coverslips were then mounted with vacuum grease (Baysilone-Paste; GE Bayer Silicones, Leverkusen, Germany) on a custom-made metallic sample holder.

SPIM setup and image acquisition

For SPIM imaging we used a custom-made setup (see *sketch* in Fig. 1 *a*) that is based on previous ideas and realizations (10,11,19,20). The 700-μm wide beam of a 491.5-nm DPSS-laser (Cobolt Calypso; Cobolt AB, Solna, Sweden) was widened by a beam expander (L1 = AC254-040-A and L2 = AC254-150-A; Thorlabs, Newton, NJ), resulting in a beam diameter of 2.63 mm. The beam was then focused in one dimension by a cylindrical lens (LJ1277L1-A; Thorlabs) onto the back-focal plane of the illumination objective (HCX APO L 10×/0.30 W U-V-I; Leica Microsystems, Mannheim, Germany) to form an elliptically deformed Gaussian beam that serves as a light sheet. Fluorescence from the sample was collected perpendicular to the illumination light sheet by a second objective (HCX APO L 40×/0.80 W U-V-I; Leica Microsystems). Fluorescence light was filtered with a single-band filter (531/46 nm, BrightLine; Semrock, Rochester, NY) and collected by a tube lens (AC508-200-A; Thorlabs) which focused the light onto the sensor of an sCMOS-camera (ORCA-Flash 4.0;, Hamamatsu Photonics, Hamamatsu City, Japan). The light sheet had a minimum waist ($1/e^2$-length) of 2.5 μm (Fig. 1 *b*). The lateral and axial extension of the setup's point-spread function was 460 nm and 1.4 μm in the light-sheet waist, respectively.

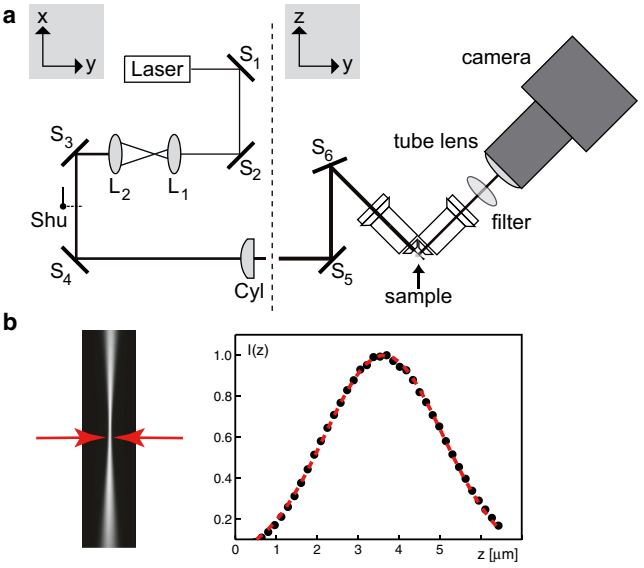

FIGURE 1 (*a*) Sketch of the beam path of the custom-made SPIM. (Please note that *all parts left from the dashed line* are shown from the *top* whereas *all parts on the right* are shown from the *side*.) Coordinate systems (*gray boxes*) indicate this change of perspective. Please see Materials and Methods for specification of all parts. (*b*) Visualization of the beam profile from the side. The light-sheet thickness at the waist (*red arrows*) shows a Gaussian profile with a full width at half-maximum of ~2.9 μm ($1/e^2$ decay length: 2.5 μm). The lateral and axial extension of the point-spread function of the setup was determined via fluorescent beads to be 460 nm and 1.4 μm in the light-sheet waist, respectively. To see this figure in color, go online.

For convenient work with *C. elegans* probes, we used water-dipping objectives that were arranged in an angle of 45° with respect to the optical table (Fig. 1 *a*). To this end, guiding mirrors and objectives were mounted on a vertical breadboard in a similar fashion to that described in Wu et al. (12) and Capoulade et al. (21). Orientation and positioning of the objectives is crucial for SPIM because the light sheet has to be aligned with the focal plane of the detection path. Therefore, the position of the detection objective was adjustable by two orthogonal linear stages (M-UMR5.16; Newport, Stratford, CT). The custom-made sample chamber was held at fixed temperature (21° C).

The sample was moved with respect to the light sheet by two motorized stages (T-LS28M-KT03; Zaber Technologies, Vancouver, British Columbia, Canada) in the *xy* direction, and by a nanopositioner (P-721 PIFOC; Physik Instrumente, Karlsruhe, Germany) in the *z* direction. Due to the limited working range of the nanopositioner, an additional manually operated stage (HT 60-5; Qioptiq Group, Rochester, NY) was used to adjust the coarse position of the probe. The precise movement of the nanopositioner was exploited for acquiring three-dimensional image stacks of the probe with a precision of a few nanometers. The setup was controlled via a custom-made LABVIEW program (National Instruments, Austin, TX), which also had an interface to the HOKAWO imaging software (Hamamatsu Photonics) that controlled the camera.

Before long-term measurements, the sample was positioned in the center of the field of view, and lower/upper borders for the *z*-stack imaging via the nanopositioner were defined. Embryos were imaged every 60 s by taking stacks of 51 sections (nanopositioner step size $\Delta = 2$ μm, 50-ms exposure time for each layer with a laser power of 0.5 mW) to allow for a full three-dimensional reconstruction of the sample. Each stack took 7–8 s due to a very conservative driving of the nanopositioner; a fivefold speedup was seen later to not compromise the quality of the data. Image stacks were aligned and processed as described below to obtain tracks of individual cells. Due to the rapid imaging, the timing of cell divisions and the orientation of division axes could also be determined (see *arrows* in Fig. 2 *c*).

Image processing

Postprocessing of raw images, i.e., aligning images within a stack, was done with a custom-made MATLAB code (The MathWorks, Natick, MA).

In the SPIM setup, samples are moved in a 45° angle with respect to the optical axis of the detection system. Two adjacent layers in an image stack with n layers are therefore laterally displaced and need to be aligned to obtain a full three-dimensional representation of the probe. Denoting the step size of the nanopositioner by Δ, the lateral displacement is

$$d = \Delta \cos\left(\frac{\pi}{4}\right) = \frac{\Delta}{\sqrt{2}}.$$

The shift in units of pixels with length ℓ is hence

$$d_p = \frac{\Delta}{(\sqrt{2}\ell)}.$$

Please note that d_p is, in general, not an integer value. For the alignment, the central layer of each stack ($k_{\mathrm{inv}} = n/2$) is chosen to be invariant. All other layers $k \neq k_{\mathrm{inv}}$ are shifted laterally by

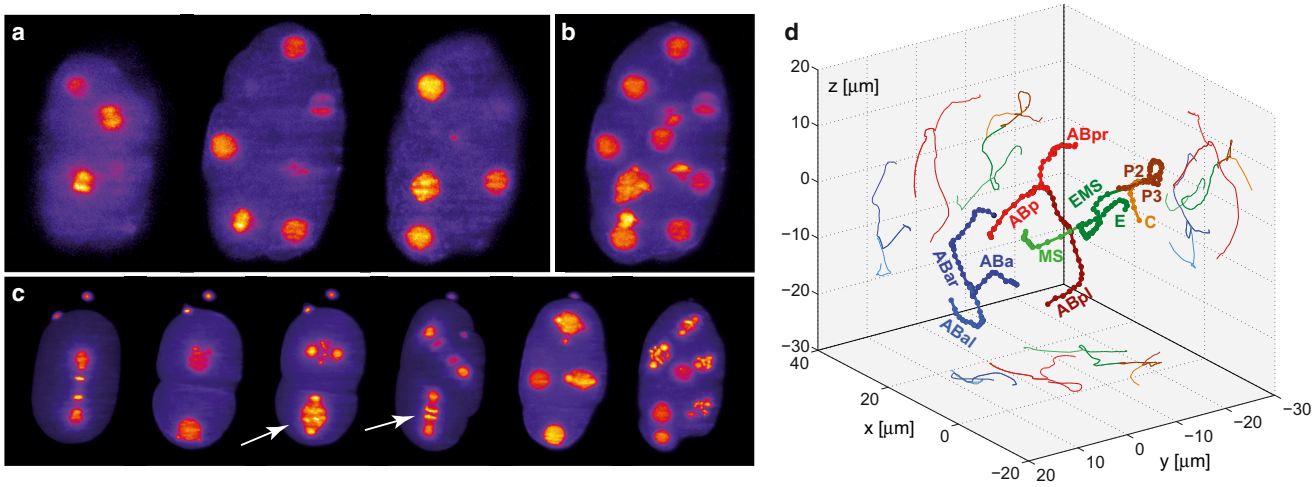

FIGURE 2 (*a*) Different optical sections of a *C. elegans* embryo (long axis ~50 μm) in the 12-cell stage. Images are raw data that have not been modified or smoothed. (*b*) Maximum projection of all sections, showing all 12 nuclei positions with a high contrast. (*c*) Maximum projection of image stacks for the same embryo in different developmental stages. (*Open arrows*) Cell divisions. (*d*) Representative example of three-dimensional cell trajectories. Cells are color-coded and named. Cell divisions are visible as branching points of trajectories. To see this figure in color, go online.

$$p_k = \left[(k_{\text{inv}} - k)\cdot d_p\right].$$

Here, square brackets denote mathematical rounding. To compensate rounding errors, each layer is moved along the respective direction by

$$s_k = (k_{\text{inv}} - k)d_p - \left[(k_{\text{inv}} - k)d_p\right] < 1$$

via interpolation with cubic splines. After alignment, stacks were cropped to relevant parts of the field of view to reduce data size.

Tracking of nuclei during development

Monitoring the movement and division of cells during early *C. elegans* embryogenesis requires an errorless tracking algorithm, i.e., no false positive or negative counts can be accepted. In addition, the assignment of nuclei in consecutive stacks must be correct, to not misinterpret trajectories. We therefore developed a tracking algorithm that can accurately achieve these goals.

To compensate for any drift of the embryo during image acquisition (due to a remnant creep of the not-yet-equilibrated agarose (22)), we first determined for each image stack the egg's center of mass that served subsequently as the origin of the coordinate system for evaluating cell tracks. To this end, we binarized each image stack by applying a threshold S_1 that separates the egg from the background. To remove stray voxels in this binary image, we applied an erosion and dilation filter each with an ellipsoidal extension 15 × 15 × 3 voxel. As a result, only one region, the volume of the egg, remained visible from which we calculated the center of mass and the ellipsoidal extension of the egg.

Next, original images in a stack were convolved with a box filter to suppress noise. Applying this filter also ensures that nuclei appear brightest in their center, which facilitates the tracking. Filtered images were searched for local intensity maxima. Voxels that were local maxima with an intensity above a threshold S_2 were set to unity; all other voxels were set to zero. To compensate for a minor bleaching during the experiment, this threshold was slightly reduced every 20 stacks. Nuclei often showed several intensity maxima that were near to each other, especially during prometaphase. To connect those, binary images were dilated with an ellipsoidal filter (size 15 × 15 × 3). Then, centroids of all remaining regions were calculated. These represent positions of the embryo's nuclei, including some false positives that were removed in a later quality-control step (see below).

To automatically connect sequential positions, the motion of nuclei between two subsequent image stacks shall not exceed half of the minimum distance between two nuclei. For our data, this criterion was easily satisfied by a lag time of $T \leq 60$ s between two successive stacks. Hence, every nucleus detected at time t can be connected to the closest nucleus position found in the stack at time $t - T$. Owing to this small time lag, there is also no need for a special treatment of cell divisions; daughter cells are simply connected to their mother cell in the previous stack. Reconstructing trajectories with this approach also allowed us to remove remaining false positives: Only full trajectories that started in the first and ended in the last stack were stored for further analysis. Because a low value of S_2 ensures that all nuclei are found, and because apoptosis is not present in early stages of development, trajectories with gaps have to be from false-positive nucleus positions and can therefore be dismissed.

Tracking data needed to be aligned for comparing different embryos because imaging of the eggs started at different time points during embryogenesis (more or less close to the anterior-posterior (AP) division of the zygote), and eggs had different orientations with respect to the light sheet. The alignment therefore included a rotation and a temporal offset. Spatial translations were not needed because all trajectories are measured relative to the eggs' center of mass. For alignment, the first image stack of the six-cell state was used due to its intrinsic asymmetry that minimizes possible ambiguities of the alignment process. Cell coordinates in one egg (i.e., the sample) were iteratively subjected to rotation matrices, and the emerging new coordinates were compared to another egg's coordinates (i.e., the reference). The rotation for which a minimal sum of absolute differences between sample and reference coordinates emerged was defined to yield the best alignment in space. Rotation matrices were sampled in 1° steps. The temporal offset was eliminated by demanding that the cumulated difference in cell number over all times had to be minimal. Using 8-, 10-, or 12-cell states for the alignment process did not lead to systematic changes, i.e., optimal rotation angles varied only slightly ($\pm 10°$) and trajectories from two different alignment processes deviated at most by ± 500 nm.

RESULTS AND DISCUSSION

To follow the early development of *C. elegans* embryos with SPIM, we used a strain that expresses GFP-tagged H2B

histones and β-tubulin (17). This double-labeling yields a bright fluorescence signal of the nucleus and the cytoskeleton that allows for a precise tracking of nuclei, cell division, and spindle axes over extended timescales (see Fig. 2, *a–c*, for representative images). Embryos were observed to hatch after imaging, i.e., the phototoxicity induced by SPIM imaging was negligible.

From our SPIM data we reconstructed three-dimensional trajectories of individual cells in several embryos (see Materials and Methods for details). Because cell lineages of *C. elegans* are invariant (23), individual cells could be identified and named (see example in Fig. 2 *d*). In line with previous observations (23), we observed that 4-, 8-, and 12-cell stages were particularly long-lived. During this time, cell motion was reminiscent of a diffusion-driven relaxation toward a closed-packing configuration within the egg shell. Moreover, cell trajectories were very similar in different embryos (see example in Fig. 3 *a*). The absolute distance Δr between trajectories in eight different embryos was on average <3.5 μm (see Fig. 3 *b*), which is $<10\%$ of the overall size of the embryo (~50 μm). In fact, the average variation, $\langle \Delta r \rangle$, is even overestimated by this approach: Embryos had different orientations with respect to the light sheet, and the timing of cell divisions also varied slightly between different embryos. Moreover, we have tracked only nuclei, i.e., a somewhat stochastic positioning of nuclei within cells contributes to the apparent trajectory variation. Estimating the latter to be in the 1–2 μm range and assuming it to be the dominant source of error, trajectory variations are reduced to $\langle \Delta r \rangle \approx$ 1–2 μm. We therefore conclude that cells move in a very deterministic fashion during early *C. elegans* development.

Based on our observations, we hypothesized that cell configurations up to the 12-cell stage (i.e., well before the onset of gastrulation) are mainly a result of mechanical cues: Cells aim to relax toward a closest packing configuration with minimized repulsive interactions. To quantitatively test this hypothesis, we asked whether a simple model of interacting and diffusing soft spheres within an ellipsoidal boundary can mimic the experimentally observed cell arrangements and trajectories in early *C. elegans* embryos. The rationale to only consider spherical cell shapes was twofold:

1. This approach certainly is the simplest possible strategy that minimizes model parameters.
2. Cells in early *C. elegans* embryos adopt a shape that is reminiscent of soft balls that have been squeezed into an ellipsoidal envelope, i.e., cells have a rather planar contact area and bulge out spherically when the egg shell is removed (16).

For the model, we then considered all cells to be spheres of radius R_i ($i = 1,\ldots, n$ denoting the cell) with a center-of-mass position $\mathbf{r}_i$. Throughout the simulation, the total volume of all cells was fixed to the egg volume. When touching the egg shell, cells experienced a repulsive force, $\mathbf{K}_i = K_0(1 - a/R_i)\mathbf{e}_n$. Here, $\mathbf{e}_n$ denotes a unit vector perpendicular to the egg shell, pointing into the egg (*red arrows* in Fig. 3 *d*, *inset*); a is the distance between the cell's position and the egg shell along $\mathbf{e}_n$. For $a > R_i$, $\mathbf{K}_i = 0$. The egg shell was modeled as an ellipsoid with axes $\ell_x = 25$ μm, $\ell_y = \ell_z = 15$ μm.

Repulsive pair-wise forces among any two cells i and j were implemented as

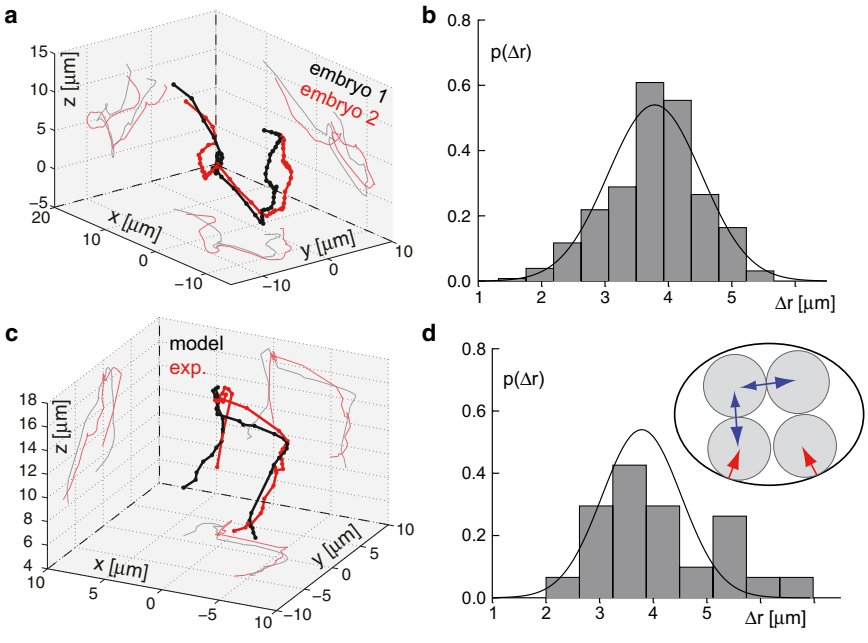

FIGURE 3 (*a*) Representative cell trajectories in two different embryos (*red* and *black*). A close similarity of both sets of trajectories is visible. (*b*) The probability distribution $p(\Delta r)$ of absolute distances Δr between cell trajectories in any two embryos reveals a low variation in cell movements (*histogram*). (*Solid lines*) Best-fitting Gaussian. As compared to the overall size of the egg (~50 μm), the average variation $\langle \Delta r \rangle \approx 3.5$ μm of cell trajectories is very small (see also main text for discussion). (*c*) Representative example of an experimental cell trajectory (*red*) and the corresponding model prediction (*black*). A close similarity between the trajectories is visible. (*d*) The probability distribution $p(\Delta r)$ of absolute deviations Δr between experimental cell trajectories and model trajectories (*histogram*) overlaps with the experimental variation of trajectories (*solid line* indicates the Gaussian in panel *b*). Thus, the model can predict cell trajectories within the experimental uncertainty. (*Inset*) Sketch of the model in which cells are taken as spheres (*gray*) that can move inside an ellipsoidal egg shell (*black line*). Repulsive forces from other cells and the egg shell are highlighted (*blue* and *red arrows*), respectively. To see this figure in color, go online.

$$\mathbf{F}_{ij} = F_0 \mathbf{e}_{ij} \begin{cases} 1 & r_{ij} \le \min(R_i, R_j) \\ \dfrac{R_i + R_j - r_{ij}}{\max(R_i, R_j)} & \min(R_i, R_j) \le r_{ij} \le R_i + R_j \\ 0 & \text{otherwise.} \end{cases}$$

Here, R_i and R_j denote the cells' radii; $r_{ij} = |\mathbf{r}_{ij}| = |\mathbf{r}_j - \mathbf{r}_i|$ is the distance between their centers; and $\mathbf{e}_{ij} = \mathbf{r}_{ij}/r_{ij}$ is the unit vector pointing from cell i to cell j. Upon approaching each other, repulsion grows linearly and is held constant upon reaching small distances. Hence, cells act as deformable balls that can squeeze each other.

Because cells lie dense within the egg shell, cell motion was assumed to be overdamped. Hence, cell positions were updated via a discretized overdamped Langevin equation (integration time step $\Delta t = 5$ s):

$$\mathbf{r}_i(t + \Delta t) = \mathbf{r}_i(t) + \frac{\Delta t}{\gamma}\left(\mathbf{K}_i + \sum_{j \neq i} \mathbf{F}_{ij}\right) + \boldsymbol{\xi}.$$

Forces were fixed via the empirically determined prefactors $K_0/\gamma = 0.2$ μm/s and $F_0/\gamma = 0.1$ μm/s. Random cell motion due to thermal effects, stochastic cytoskeleton movements, etc., are summarized by a random increment vector $\boldsymbol{\xi}$ whose components are uncorrelated random numbers with zero mean and variance 0.027 μm^2 (parameter determined empirically). Therefore, cells undergo a diffusive motion and experience deterministic repulsive forces $\mathbf{K}_i$ and $\mathbf{F}_{ij}$. Varying force parameters in the range K_0/γ, $F_0/\gamma = 0.01,\ldots,$ 1 μm/s did not lead to gross changes of the resulting cell configurations. In particular, increasing the ratio K_0/F_0 only accelerated cell migration, i.e., final cell positions were reached faster. Increasing K_0 at fixed F_0 leads to a stronger repulsion of cells from the ellipsoidal shell, which altered cell migration timing slightly and led to a more compressed configuration of cells. Strength of the random force $\boldsymbol{\xi}$ could be varied >10-fold without affecting the configurational outcome. Again, only migration timing varied, albeit much less as compared to changes in F_0 and K_0. Based on these observations, we chose the above stated parameter values in such a way that experimentally observed cell configurations were reproduced and cells migrated to these positions as slowly as possible but with a minimum deviation from experimental trajectories.

The equations of motion can only be applied to a fixed number of cells, n, because cell divisions are not included in the model. Moreover, we did not observe any significant correlation between experimentally determined cell division axes and directions of minimal forces. Therefore, cell division events were considered by including average division times and axes as determined from our SPIM data. Radii of daughter cells were chosen to be identical for symmetric divisions whereas, for asymmetric divisions, we assumed a volume ratio of 2:3.

As a first test of the model, we compared experimentally obtained three-dimensional trajectories of cells with those obtained from the model. Please note that cell division timing and division axis orientation (as determined from images in the metaphase) are trivially identical, because they have been taken as input for the model. Trajectories of cells between divisions, however, are a genuine result of the model that have not been predetermined. If the model was not capable of describing the experimental system, a rapid divergence of simulated and experimentally observed trajectories was anticipated. Strikingly, however, the model's trajectories follow closely the experimental cell positions (Fig. 3 *c*). Deviations are well within the experimental variation (Fig. 3 *d*), i.e., the purely mechanical interaction of cells is fully sufficient to describe the dynamics of all experimentally observed cell arrangements. Despite the biochemically determined division times and mitotic axes, the macroscopic arrangement of the early developing tissue is hence fully governed by mechanical interactions and a relaxation toward a closest cell packing.

We would like to emphasize that model parameters were uncritical, i.e., similarly good trajectory overlaps were observed when varying the force and noise parameters (see above). We also observed the same cellular arrangements when perturbing the division timing ($\pm$500s, corresponding to half a cell cycle of ABa and ABp cells). The precise timing for divisions is therefore of minor importance for proper embryogenesis as long as the sequence of cell divisions is respected. Randomizing spindle axes, however, lead to completely different trajectories of individual cells. Despite these wrong tracks of individual cells, the overall pattern of cellular positions was conserved, i.e., experimentally observed cell positions were occupied by misplaced individuals (such as ABa sitting on the position at which ABp is expected). This result highlights that the gross cellular arrangement is solely determined by mechanical constraints.

As a nontrivial result, the model predicted a planar, diamond-like arrangement of cells in the four-cell stage for all tested parameters (Fig. 4, *a* and *b*). This configuration features a maximum distance between cells and hence minimal repulsive forces. In favorable agreement with this robust model prediction, planar four-cell stages have been observed in many experiments with *C. elegans* embryos (23). Thus, mechanical rather than biochemical cues appear to be responsible for a planar four-cell stage.

A second model prediction concerns the formation of the dorsal-ventral (DV) body axis that is established when the embryo reaches the four-cell stage. In agreement with Gönczy and Rose (23), we observed in our SPIM data that the AB cell featured an initial spindle orientation perpendicular to the anterior-posterior (AP) axis of the embryo. During anaphase, the spindle rotated toward the AP axis, presumably due to repulsive interactions with the egg shell. As a result, an anterior and a posterior daughter cell (ABa

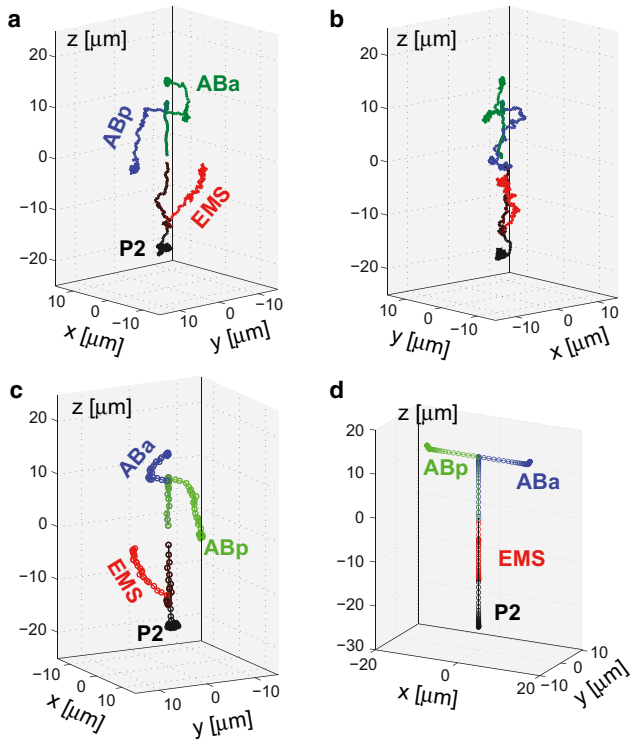

FIGURE 4 In agreement with experimental observations, the model predicts a planar four-cell stage (*a*, *front view*; *b*, *side view*). (*c*) Formation of the dorsal-ventral axis, set by a direct contact of ABp and P2 cells, is well captured within the model. (*d*) T-like cell configuration without the repulsive forces of the egg shell. In line with experimental results, a misalignment of cells as compared to the native state is observed. To see this figure in color, go online.

and ABp) emerge. Concomitant to AB division, the P1 cell divides along the AP axis into the P2 and EMS cells so that ABp and P2 eventually touch each other and hence define the DV axis (23).

In the model, we restricted AB division to occur perpendicular to the AP axis and followed the trajectories of the equally sized daughter cells. In all cases we observed that one daughter cell moved toward an anterior position (hence being ABa) whereas the other daughter cell migrated to the ABp position at which the spontaneous contact with P2 defined the DV axis (Fig. 4 *c*). Key to this spontaneous (noise-induced) symmetry breaking between AB's daughter cells is the egg shell's repulsive force that guides the migration of ABa and ABp migration. These model results are in favorable agreement with experimental observations: Removing the egg shell has been shown to block spindle reorientation during AB division, and hence leads to failure in DV axis formation (15). We therefore conclude that formation of the DV axis is dominantly driven by mechanical interactions that guide cells to the right position in the embryo.

Cell divisions in the planar four-cell stage finally determine the right-left body axis. Key to this event is a division of ABa and ABp cells with a division axis almost perpendicular to the planar cell arrangement (23). Owing to the GPA-16 gene, spindle axes are slightly rotated before cytokinesis to allow for a more anterior positioning of the daughter cells ABal and ABpl as compared to their more posterior siblings ABar and ABpr (24). This slight shift eventually defines the left-right axis (23). Knocking down the GPA-16 gene blocked the slight rotation of the spindle and resulted in a random distribution of left and right (24). In line with this experimental observation, avoiding a biasing tilt of division axes in ABa and ABp in our model also leads to a randomization of left and right (data not shown).

Finally we probed the cell arrangement that arises in early *C. elegans* embryos without the guidance of an egg shell. Experimentally, a T-like arrangement of ABa, ABp, EMS, and P2 had been observed (15) when removing the egg shell. Indeed, our model nicely reproduces this result (Fig. 4 *d*), hence underlining that sterical interactions among cells but also repulsion via the egg shell are crucial determinants for a proper development of *C. elegans*. Because our model did not include cell adhesion, considering random forces without a confining egg shell would lead rapidly to a random dispersion of cells. We therefore only considered deterministic repulsive forces between cells in this simulation. Because they cease as soon as cells no longer overlap, cells stayed near to each other after reaching their equilibrium position. Due to that, cell trajectories in simulations without egg shell appear as deterministic, straight paths (Fig. 4 *d*). Nevertheless, even this very simple approach can reproduce the experimentally observed phenotype.

Clearly, the model investigated here is simplified in three aspects:

1. Cell adhesion is not explicitly taken into account, but cells stay together via repulsive forces imposed by the confining egg shell. Although this approach works nicely for intact eggs (see above for a comparison), a refined model certainly will have to account for cell adhesion because removal of the egg shell, for example, does not induce disassembly of the emerging embryonal tissue (16).
2. More details about intercellular forces need to be included because collective cell migration has been shown to rely mostly on tensile forces that can be quite heterogeneous from cell to cell (see, for example, Trepat and Fredberg (25), for a recent review).
3. Intracellular events that determine the cells' division axis, e.g., PAR protein gradients (23), need to be included to arrive at a true self-organization model that integrates both mechanical and biochemical cues. The approach shown here hopefully will serve as a valuable starting point in this endeavor.

CONCLUSION

In summary, we have used SPIM in combination with a simple mechanical model to quantitatively describe the early

steps of *C. elegans* embryogenesis. The good agreement between the model and experimental observations support the hypothesis that tissue organization in early stages of *C. elegans* embryogenesis is strongly guided by mechanical cues whereas later developmental stages are more dependent on morphogen-driven pattern formation.

We thank I. Mattaj for *C. elegans* strains, P. Rupprecht and K. Weidner-Hertrampf for help with sample preparation, and L. Hufnagel, J. Huisken, P. J. Keller, U. Krzic, and F. Pampaloni for helpful discussions on SPIM.

REFERENCES

1. Turing, A. M. 1952. The chemical basis of morphogenesis. *Philos. Trans. R. Soc. Lond., B.* 237:37–72.
2. Nakamasu, A., G. Takahashi, …, S. Kondo. 2009. Interactions between zebrafish pigment cells responsible for the generation of Turing patterns. *Proc. Natl. Acad. Sci. USA.* 106:8429–8434.
3. Baena-Lopez, L. A., X. Franch-Marro, and J. P. Vincent. 2009. Wingless promotes proliferative growth in a gradient-independent manner. *Sci. Signal.* 2:ra60.
4. Grill, S. W. 2010. Cell biology. Forced to be unequal. *Science.* 330:597–598.
5. Aegerter-Wilmsen, T., M. B. Heimlicher, …, K. Basler. 2012. Integrating force-sensing and signaling pathways in a model for the regulation of wing imaginal disc size. *Development.* 139:3221–3231.
6. Aegerter-Wilmsen, T., A. C. Smith, …, K. Basler. 2010. Exploring the effects of mechanical feedback on epithelial topology. *Development.* 137:499–506.
7. Hufnagel, L., A. A. Teleman, …, B. I. Shraiman. 2007. On the mechanism of wing size determination in fly development. *Proc. Natl. Acad. Sci. USA.* 104:3835–3840.
8. Puliafito, A., L. Hufnagel, …, B. I. Shraiman. 2012. Collective and single cell behavior in epithelial contact inhibition. *Proc. Natl. Acad. Sci. USA.* 109:739–744.
9. Schoeberl, B., C. Eichler-Jonsson, …, G. Müller. 2002. Computational modeling of the dynamics of the MAP kinase cascade activated by surface and internalized EGF receptors. *Nat. Biotechnol.* 20:370–375.
10. Keller, P. J., A. D. Schmidt, …, E. H. Stelzer. 2008. Reconstruction of zebrafish early embryonic development by scanned light sheet microscopy. *Science.* 322:1065–1069.
11. Huisken, J., J. Swoger, …, E. H. K. Stelzer. 2004. Optical sectioning deep inside live embryos by selective plane illumination microscopy. *Science.* 305:1007–1009.
12. Wu, Y., A. Ghitani, …, H. Shroff. 2011. Inverted selective plane illumination microscopy (iSPIM) enables coupled cell identity lineaging and neurodevelopmental imaging in *Caenorhabditis elegans*. *Proc. Natl. Acad. Sci. USA.* 108:17708–17713.
13. Krzic, U., S. Gunther, …, L. Hufnagel. 2012. Multiview light-sheet microscope for rapid in toto imaging. *Nat. Methods.* 9:730–733.
14. Huisken, J., and D. Y. R. Stainier. 2009. Selective plane illumination microscopy techniques in developmental biology. *Development.* 136:1963–1975.
15. Edgar, L. G., N. Wolf, and W. B. Wood. 1994. Early transcription in *Caenorhabditis elegans* embryos. *Development.* 120:443–451.
16. Lee, J. Y., and B. Goldstein. 2003. Mechanisms of cell positioning during *C. elegans* gastrulation. *Development.* 130:307–320.
17. Askjaer, P., V. Galy, …, I. W. Mattaj. 2002. Ran GTPase cycle and importins α and β are essential for spindle formation and nuclear envelope assembly in living *Caenorhabditis elegans* embryos. *Mol. Biol. Cell.* 13:4355–4370.
18. Bao, Z., and J. I. Murray. 2011. Mounting *Caenorhabditis elegans* embryos for live imaging of embryogenesis. *Cold Spring Harb. Protoc.* 10.1101/pdb.prot065599.
19. Siedentopf, H., and R. Zsigmondy. 1902. About the visual and size specifications of ultramicroscopy particles, with particular application to gold ruby glasses [Ueber sichtbarmachung und groessenbestimmung ultramikoskopischer teilchen, mit besonderer anwendung auf goldrubinglaeser]. *Annalen der Physik.* 315:1–39.
20. Voie, A. H., D. H. Burns, and F. A. Spelman. 1993. Orthogonal-plane fluorescence optical sectioning: three-dimensional imaging of macroscopic biological specimens. *J. Microsc.* 170:229–236.
21. Capoulade, J., M. Wachsmuth, …, M. Knop. 2011. Quantitative fluorescence imaging of protein diffusion and interaction in living cells. *Nat. Biotechnol.* 29:835–839.
22. Keller, P. J. 2013. In vivo imaging of zebrafish embryogenesis. *Methods.* 62:268–278. http://dx.doi.org/10.1016/j.ymeth.2013.03.015.
23. Gönczy, P., and L. S. Rose. 2005. Asymmetric cell division and axis formation in the embryo. *WormBook.* Oct 15:1–20.
24. Bergmann, D. C., M. Lee, …, W. B. Wood. 2003. Embryonic handedness choice in *C. elegans* involves the Gα protein GPA-16. *Development.* 130:5731–5740.
25. Trepat, X., and J. J. Fredberg. 2011. Plithotaxis and emergent dynamics in collective cellular migration. *Trends Cell Biol.* 21:638–646.